Mechanical and Electromagnetic Waves

Matthew Evans

27$^{\text{th}}$ March 2019

Various wave properties were investigated by exploring water waves in a ripple tank and studying the diffraction of laser light. A value of 0.18 ± 0.05 ms^{-1} for water wave speed at varying frequencies and a fixed depth of $h = 1.0 \pm 0.3$ cm was obtained and the one generated by using $v \approx \sqrt{gh}$ [4] was 0.3 ± 0.1 ms^{-1}. The angles of incidence and reflection for the reflection of water waves at a barrier were found to be $41 \pm 2°$ and $41 \pm 2°$ respectively. The water wave speed was also investigated at a fixed frequency of 20 Hz with varying depths allowing a value of 4.4 ± 0.1 ms^{-2} for the acceleration due to gravity to be determined with the known value as 9.8 ms^{-2}. The value for the wave speed at varying frequencies was different to the one expected lying outside the uncertainty range, also the value of g was different to the known value however, the angle of incidence and reflection were shown to be equal to each other. Experimental values determined for the wavelength of the laser light source for the single and double-slit configurations was found to be 652.1 ± 0.7 nm and 655.71 ± 0.03 nm respectively, using a 0.3mm aperture, a slit width of $a = 0.04$ mm and slit separation of $d = 0.5$ mm: the value of the device is 650 ± 10 nm [8]. These values compare well with the device value along with other single and double-slit configurations generating wavelengths that compared well with the device value but, all the uncertainties of the experimental values of the wavelength were underestimated. By understanding water waves and electromagnetic waves, hydroelectric power and chemical spectra analysis could be optimised for the benefit of many modern day appliances.

1   Introduction

The various properties and characteristics of waves were investigated in these experiments. These physical phenomena are at the heart of many transmission processes; such as the propagation of sound through a medium responsible for audio communication and the transmission of electromagnetic (EM) waves in a vacuum which enables visible light from the Sun to travel to Earth. In addition, quantum mechanics has made the connection between the wave-like nature exhibited by particles and the particle-like nature of waves. Interesting developments have been made due to the study of waves and this is at the forefront of modern technologies.

A wave can be thought of as a time-varying disturbance that propagates through a medium or a vacuum. This can be described mathematically as a wave function $\psi(x, t)$

$$\psi(x, t) = \psi_0 cos(kx - \omega t) \tag{1}$$

where, ψ_0 is the wave amplitude, x is the spatial position of the propagating wave at time t, k is the wave vector related to the wavelength, λ by $k = 2\pi/\lambda$, and ω is the angular frequency related to the time period, T, of the wave by $\omega = 2\pi/T$. Equation (1) only considers the real part of the propagating wave. In most instances, waves also have an imaginary part. From Euler's identity equation (1) can be re-expressed as a complex exponential

$$\psi(x, t) = \psi_0 e^{i(kx - \omega t)} \tag{2}$$

and all the symbols have their usual meaning as defined for equation (1).

The various characteristics of waves is the same for different types of waves [1]. Making use of this physical concept, the first of these experiments investigates wave phenomena using mechanical water waves in a ripple tank. In particular reflection, refraction, diffraction and interference were studied. The latter two phenomena were investigated further in the second experiment where a laser light was diffracted through single and double slits to investigate interference and diffraction patterns. Furthermore, extensions to these experiments looked into other wave phenomena such as the dependence of water wave speed with depth and how interference patterns of EM waves could be used to determine the wavelength of a light source.

2   Theory

The speed of waves, v, can be determined by using

$$v = \lambda f \tag{3}$$

where λ is the wavelength and f is the frequency of the waves - the number of waves that pass a given point per second. However, the speed of mechanical waves often depend upon the medium which they travel, in addition to many other factors. For water waves, the speed depends on depth. For shallow depths, this is given by [4]

$$v \approx \sqrt{gh} \tag{4}$$

where g is the acceleration due to gravity and h is the measured depth of the water used in the ripple tank. For the interested reader, a more detailed analysis of water waves can be found at [4].

When a wave front approaches at an angle to a boundary reflection occurs. This is when the angle of incidence, θ_i is equal to the angle of reflection, θ_r at the boundary

$$\theta_i = \theta_r \tag{5}$$

Figure 1 describes this pictorially.

If the wave passes between two different media and changes speed, as a consequence, it will change direction. This is known as refraction. Figure 1 shows a physical representation for this phenomena.
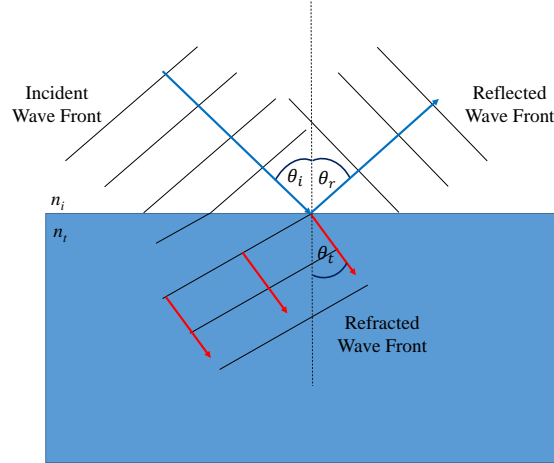

Figure 1: A diagram demonstrating the physical processes of reflection and refraction as an incident wave front encounters a boundary. The direction of travel for the incident and reflected waves are shown by the blue arrows, whilst the direction of travel for the refracted wave is shown by the red arrows. The two media have refractive indices n_i and n_t. The angles, θ_i, θ_r and θ_t correspond to the angles of incidence, reflection and refraction respectively between direction of travel and the normal to the boundary.

Diffraction occurs when a wave 'bends' as it passes through a gap (or slit) between two obstacles or when the wave travels around a barrier. An illustration for the diffraction of light is given in Figure 2 when incident light waves encounter a single slit.
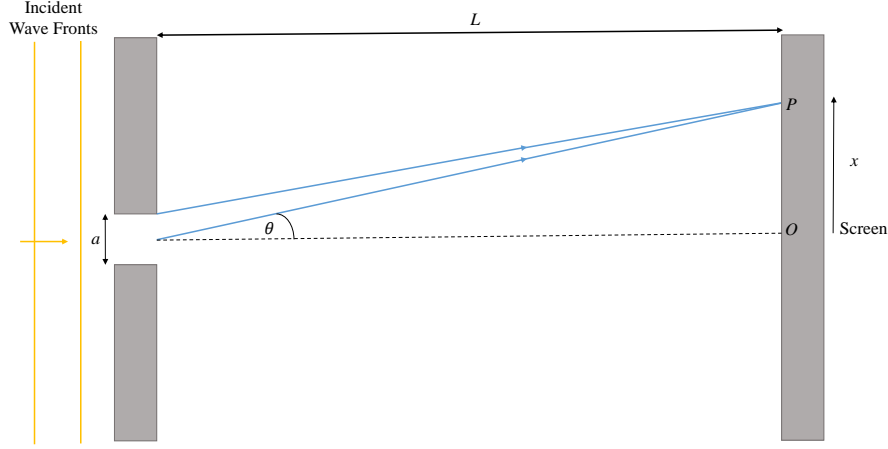
Figure 2: An illustration demonstrating the diffraction of light from a single slit and defining some terms. The incident light wave approaches a slit of width a and two beams are considered from the Huygen's wavelets [3] formed as a result of passing through the slit. These two beams arrive at a point P creating an interference pattern on the screen and the bottom ray is diffracted through by an angle θ. The distance between the plane of the slit and the screen is L and the vertical distance (position on the screen) between the origin, O and point P is x.

The intensity of diffracted light from a single slit into an angle θ [2] is given by

$$I = I_0 \frac{sin^2\alpha}{\alpha^2} \tag{6}$$

where $\alpha = (\pi a sin\theta)/\lambda$, λ is the wavelength of the light and a is the slit width.

For two slits, the intensity of diffracted light into an angle θ [2] is

$$I = I_0 \frac{sin^2\alpha}{\alpha^2} cos^2\delta \tag{7}$$

where $\delta = (\pi d sin\theta)/\lambda$ and d is the separation distance between the two slits. A derivation for equations (6) and (7) involving a geometrical approach and phasor diagrams can be found from [3]. These equations can also be dervied by considering Fourier transforms and the convolution theorem and approach using these techniques can be found from [7].

For the experimental configuration that was considered, the small angle approximation could be used. Therefore the single slit intensity equation (6) can be re-expressed as

$$I \approx I_0 \frac{sin^2 \frac{\pi a x}{L\lambda}}{\left(\frac{\pi a x}{L\lambda}\right)^2} \tag{8}$$

where the intensities are normalised so, $I_0 = 1$ and L is the slit to screen separation distance and x is the screen position ($L >> x$).

Similarly, the double slit intensity equation (7) can be re-expressed due to to the small angle approximation

$$I \approx I_0 \frac{sin^2 \frac{\pi a x}{L\lambda}}{\left(\frac{\pi a x}{L\lambda}\right)^2} cos^2 \frac{\pi d x}{L\lambda} \tag{9}$$

where again the intensities are normalised in the experiments so $I_0 = 1$ and all the other symbols have their usual meaning with $L >> x$.

Using equation (6), the intensity minima for a single slit occurs when α is a multiple of π. This therefore means that

$$sin\theta = \frac{m\lambda}{a} \quad , \quad (m = \pm 1, \pm 2, ...) \tag{10}$$

If L'Hôpital's rule [3] is applied to equation (6) in the limit as the intensity at $\alpha \to 0$ is found to be $I = I_0$ as expected. When the detector to slit distance is big, the small angle approximation can be used. Equation (10) can then be approximated to

$$\theta \approx \frac{m\lambda}{a} \quad , \quad (m = \pm1, \pm2, ...) \tag{11}$$

The intensity maxima of a single slit diffraction pattern can be approximately found by using equation (6) and realising that they occur when the sine function is a maximum (±1) [3]. In other words, when

$$\alpha = \pm\left(m + \frac{1}{2}\right)\pi \quad , \quad (m = 0, 1, 2, ...) \tag{12}$$

However, upon further analysis of applying differentiation to equation (6) and setting equal to zero to find the maxima it is found that the there is no maxima at $m = 0$ [3]. Therefore, when equation (12), with $m \neq 0$, is subsituted into equation (6) the intensity maxima, I_m is approximately given by [3]

$$I_m \approx \frac{I_0}{\left(m + \frac{1}{2}\right)^2 \pi^2} \quad , \quad (m = \pm1, \pm2, ...) \tag{13}$$

3 Method

3.1 Mechanical Waves

The ripple tank was placed on an up-turned crate and the camera was carefully mounted on the tripod directly above the ripple tank. These factors were needed to ensure that the camera set-up was in the best possible position for obtaining the required images of the water waves. Then the height of the tripod was noted along with the camera 'zoom' focus in order to keep consistency when taking photographs of the waves generated. The tray was then partially filled with water up to the sloping part of the foam [1] to reduce reflections from the edges. The depth of the water was then measured using a ruler and the uncertainty noted. This was found to be 1 ± 0.3 cm and was required for later analysis. Then a stroboscopic LED was used illuminate this from underneath the tray. The stroboscopic LED 'froze' the movement of the waves so that these can be captured by the camera and the resulting images can then be analysed. Figure 3 shows how the images of the travelling wave fronts were generated from the ripple tank.
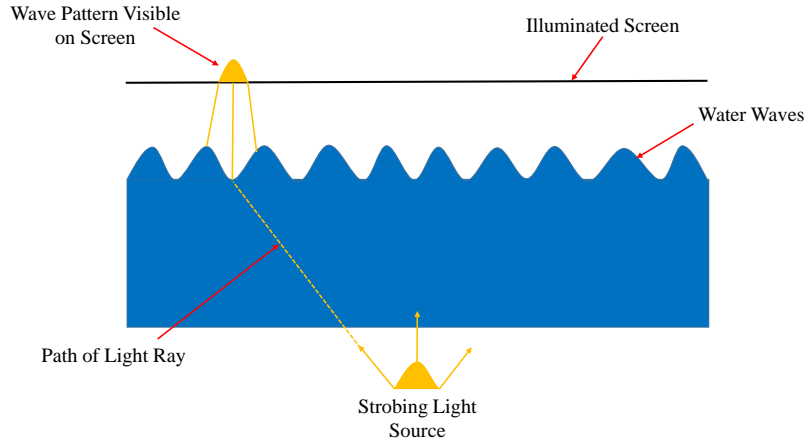

Figure 3: A side-view of the ripple tank. This shows how the strobing light source in conjunction with the generated waves produced images on the screen, placed directly above the ripple tank. The crests of the water waves absorb more light than the troughs. Hence, the bright wave fronts on the screen (shown by the yellow peak) represent the troughs of the water waves and the dark bands on the screen represent the crests of the water waves. A camera was set-up directly above the screen to capture images of the resulting wave fronts.

The frequency of the vibrator was first set to 20 Hz. The height of the dipper was carefully adjusted so that the best quality images were obtained from the camera. These images were then converted to distances in centimetres (cm) using an image processing program. A calibration image was taken of a ruler by the camera to get a conversion between image distance and 'real' distance. The uncertainties in the image processing program for the image distances were noted and these were also converted to real distances. Figure 4 shows the calibration image used.
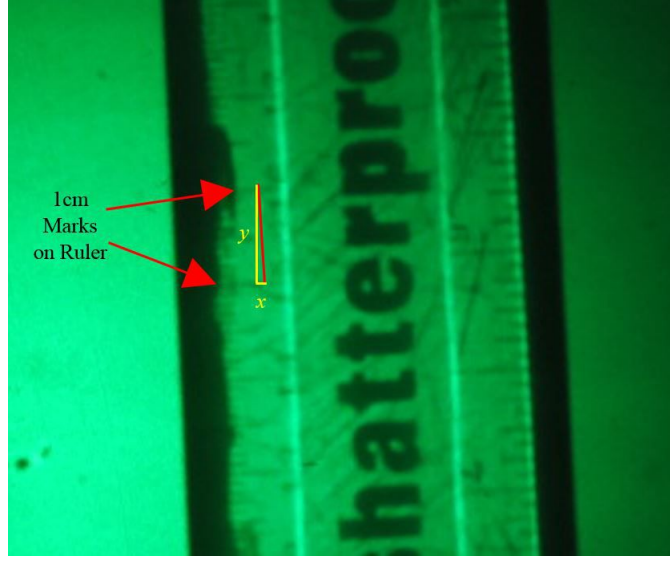
Figure 4: A photograph of a ruler was used to convert the image distances to real distances from the camera. The points between a 1cm mark on the ruler were measured in the image processing program and the distance noted. Then this was used as a conversion factor to find the wavelengths of subsequent images taken of the wave fronts in the experiment. x and y are the image distances and these were used to determine the length of the red line which corresponds to 1cm in real distance.

By using the x and y image program distances the length of the red line that corresponds to 1cm in real distance in Figure 4, was determined using

$$d' = \sqrt{x^2 + y^2} \tag{14}$$

where d' is the image program distance. All image distances, d' were divided by a conversion factor, R i.e.

$$d = \frac{d'}{R} \tag{15}$$

to gain the real image distance, d, in centimetres. The conversion factor was found to be $R = 0.66 \pm 0.01$ cm which corresponded to 1 cm in real distance. Equation (15) was then propagated through to obtain the associated errors in 'real' distance, δd using

$$\delta d \approx \frac{\delta d'}{R} \tag{16}$$

where $\delta d'$ is the uncertainty in the image distances. The term involving the uncertainty in the conversion factor, δR, could be neglected as these values were small and did not contribute much to the overall uncertainties for the 'real' distances δd.

Various different objects and obstacles were placed in the water enabling various wave phenomena to be investigated:

1. **The speed of water waves:** Plane waves generated from the vibrator were investigated to determine the wavelength of the waves at different frequencies. Three images were obtained for each frequency to gain more reliable results. The wavelengths were then found by using the image processing program in conjunction with equation (14). Then, an average of the three wavelengths for each frequency was obtained, along with propagation of the associated uncertainties, to gain a more reliable value for the wavelength. These wavelengths were then converted to real distances using equation (15) and the uncertainties were also obtained. The speed of the water waves was then determined by plotting a graph of wavelength, λ against inverse frequency (time), $1/f$. This was then compared to the theoretical value of water waves in shallow depths calculated by using equation (4).

2. **Reflection:** A barrier was placed in the tray at an angle to the incident wave fronts. The angle of incidence, θ_i and angle of reflection, θ_r was then measured (using an image processing program) to verify relation (5) for 20 Hz waves. In addition, lower frequency wave fronts were also investigated qualitatively to see how reflection changed at different frequencies.

3. **Refraction:** The velocity of water waves depend on the depth. Therefore, an object was be placed underwater and this resulted in a change of velocity of the water waves as they passed over it. This caused a change in direction of the waves and hence refraction could be investigated.

4. **Single-slit interference:** A barrier with a gap was placed in front of the dipper [1]. The gap width was then changed and the camera was used to take pictures at these different widths. In addition, the frequency was also adjusted while keeping the gap width fixed to investigate this further. Images of the maxima and minima from the resulting interference patterns were then studied.

5. **Double-slit interference:** Two gaps were created from barriers in the tray and the Young's fringes generated from the interference patterns were investigated.

6. **Wave Speed as a Function of Depth:** As a preliminary experiment, the water tray was sloped on an angle so that the water was at various depths in the tray. Then a series of images were taken to qualitatively see how the wave speed varied with depth. Once the preliminary experiments had taken place, the tray was emptied and returned to a horizontal position. To ensure that the tray was horizontal, a spirit level was used. The tray was carefully re-filled with water and a vernier calliper clamped to a tripod was used to measure different water depths in the tray. This was required so that the wave speed at a fixed frequency, of 20 Hz, could be investigated at various depths. Five depths were investigated: 0.2 mm, 0.4 mm, 0.6 mm, 0.8 mm and 1.0 mm. These depths were chosen so that the water did not overspill from the tray. Using similar techniques for investigating the speed of water waves at different frequencies and fixed depth, a camera was used to take an image for each depth. Three wavelengths were measured from each image using an image processing program and the average was taken to achieve a more accurate result. Then, by using the conversion factor (15), the wavelengths could be converted to real values along with the associated uncertainties using equation (16). The wave speed at each depth was then determined by using equation (3) and a graph of v vs $\sqrt{h}$ as then plot in order to determine a value for g, the acceleration due to gravity using equation (4).

3.2   Electromagnetic Waves

By investigating various diffraction and interference patterns of EM waves an experimental value for the wavelength of the laser light source could be determined and compared to the known value for the device: 650 ± 10 nm [8]. To achieve this, a rotating slit wheel with various slits was used along with a light sensor which had a variable aperture connected to a computer via an interface box allowed position and intensity readings to be stored. All the settings were then set-up on the computer software in order to obtain the relevant experimental data: the position (x) and received intensity (I).

Before any measurements were obtained two preliminary measurements were taken. First, the background intensity was recorded from the sensor and was then used to correct the subsequent intensity readings. Then the laser light was used to illuminate the sensor with the aperture open at a maximum (and with no slit wheel in place) so that it was receiving close to 100% intensity [1]. This was to check that the laser was operating correctly.

After the preliminary measurements were taken, the experiment was first set-up as shown in Section 2 Figure 2. The slit wheel placed at a length if $L = 0.5$ m from the screen to investigate diffraction patterns for a single slit. This length was then kept fixed throughout all the subsequent experiments. A light sensor mounted on a lateral slider was connected to a computer via an interface box. This sensor was placed at the screen distance from the single slit as shown in Figure 2. The lateral slider could then be used to carefully slide the sensor across the length of the screen, in the 'x' direction indicated in Figure 2. The interface box then recorded the sensor's position and received intensity and stored this on the computer for further analysis. This experiment was repeated for different slit widths and sensor aperture sizes to investigate the intensity at various positions in more detail.

Once the appropriate investigations for the single slit at various widths and aperture sizes had been investigated, double slit interference patterns were investigated. The experiment was adjusted so, the set-up was as shown in Figure 5.
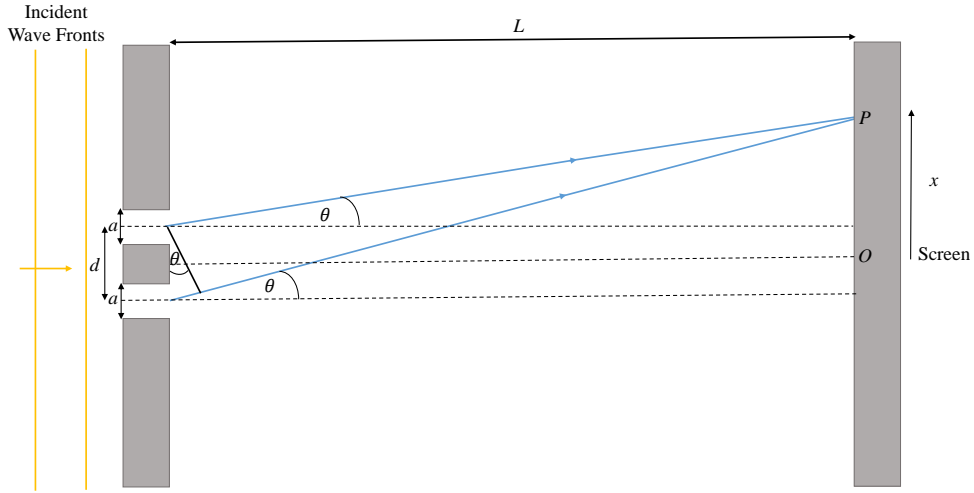
Figure 5: An illustration demonstrating the diffraction of light from double slits and defining some terms. The incident light wave approaches two slits of width a separated by a distance d. The two beams are considered from the Huygen's wavelets [3] formed as a result of passing through the slits. These two beams from the slits are assumed to be parallel as $L \gg x$ and arrive at a point P creating an interference pattern on the screen. The rays are diffracted through by an angle θ. The distance between the plane of the slit and the screen is L and the vertical distance (position on the screen) between the origin, O and point P is x.

As for the single slit experiment, a sensor on a lateral slider was used to measure the position and corresponding intensities of the diffraction patterns. Different slit widths and separations along with different sensor aperture sizes were used to investigate the resulting interference patters generated from the diffracted laser light.

Once all the position and intensity sets had been obtained for each slit configuration, the intensity positions were shifted by an amount so that the maximum intensity for the results set was positioned at the origin. The intensity readings were then normalised by dividing all the readings by the maximum intensity in the specific set and hence the maximum intensity was $I_0 = 1$. These normalised readings were then plot as a graph of intensity vs (shifted) position. Using a non-linear least squares fit, a function similar to equation (8) was fitted to the data for the single slit readings. This allowed the wavelength to be the only free parameter in equation (8) and an experimental value could then be determined along with the associated uncertainty from the fitting procedure. Similarly, a function similar to equation (9) was fitted to the double slit data along with a single slit envelope function (given by equation (9)). This allowed more experimental values of the wavelength of the laser source to be determined.

4 Results

4.1 Mechanical Waves

Figure 6 visually shows how the wavelength of plane (water) waves varied at two different frequencies of 15 Hz and 20 Hz.
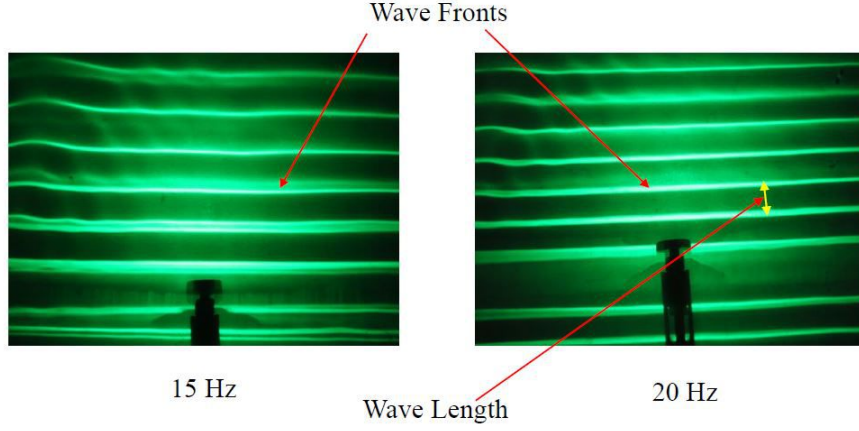
Figure 6: An image showing the wavelengths of plane waves generated by the ripple tank at 15 Hz (left) and 20 Hz (right). By taking images of plane waves at different frequencies the wave speed could then be determined.

By measuring the wavelengths of the plane waves at different frequencies as shown in Figure 6, Figure 7 shows the resulting plot of measured wavelength against time $(1/f)$ at a fixed depth of 1 ± 0.3 cm.
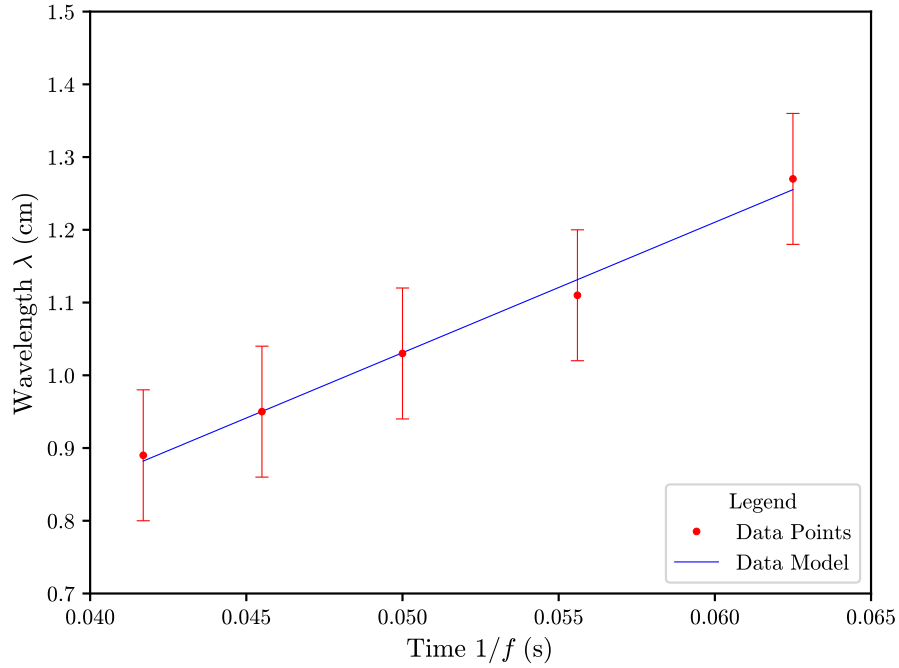

Figure 7: A plot of wavelength, λ against time $1/f$ at a fixed water depth of 1.0 ± 0.3 cm.

The gradient was determined from Figure 7 and by using equation (3) the speed of the water waves was determined. The error in the gradient was used to obtain the associated uncertainty for the wave speed. Table 1 shows the water wave speed obtained from Figure 7 and compares this to the theoretical value obtained by using equation (4) for a depth of $h = 1.0 \pm 0.3$ cm.

Table 1: Table of values for the speed of water waves at a fixed depth of $h = 1.0 \pm 0.3$ cm and varying frequency.

Value	Water Wave Speed, $v(\text{ms}^{-1})$
Experimental	0.18 ± 0.05
Theoretical	0.3 ± 0.1

Figure 8 demonstrates how water waves reflect from a boundary placed at an angle to the incident wave fronts.
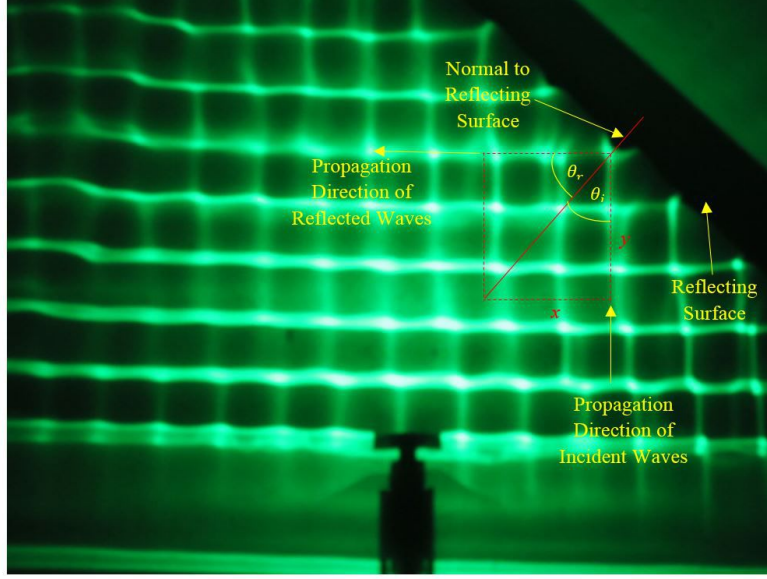
20 Hz

Figure 8: An annotated image showing the reflection of water waves at a frequency of 20 Hz due to a boundary. By measuring the image distances x and y the angle of incidence θ_i and the angle of reflection θ_r could then be determined.

From using Figure 8 the angle of incidence could quantitatively be obtained by using the relation

$$\theta_i = arctan\left(\frac{x}{y}\right) \tag{17}$$

where x and y are the horizontal image distances measured using an image processing program as described in Section 3.1 and shown in Figure 8. Then by using appropriate propagation of errors

$$\delta\theta_i = \sqrt{\left(\frac{y}{y^2 + x^2}\right)^2 (\delta x)^2 + \left(\frac{x}{y^2 + x^2}\right)^2 (\delta y)^2} \tag{18}$$

where δx and δy are the errors in the horizontal and vertical image distances respectively the associated uncertainty for the angle of incidence was determined. Relations similar to (17) and (18) were used to determine the angle of reflection, θ_r, and its associated uncertainty, $\delta\theta_r$ respectively. Table 2 shows the obtained values for the angle of incidence and reflection from Figure 8.

Table 2: Table of values for the angle of incidence and reflection for water waves at 20 Hz shown in Figure 8.

Angle of Incidence, θ_i (°)	Angle of Reflection, θ_r (°)
41 ± 2	41 ± 2

Figure 9 is two images demonstrating the refraction of water waves as they pass over a submerged semi-circular object at different frequencies of 15 Hz and 20 Hz.
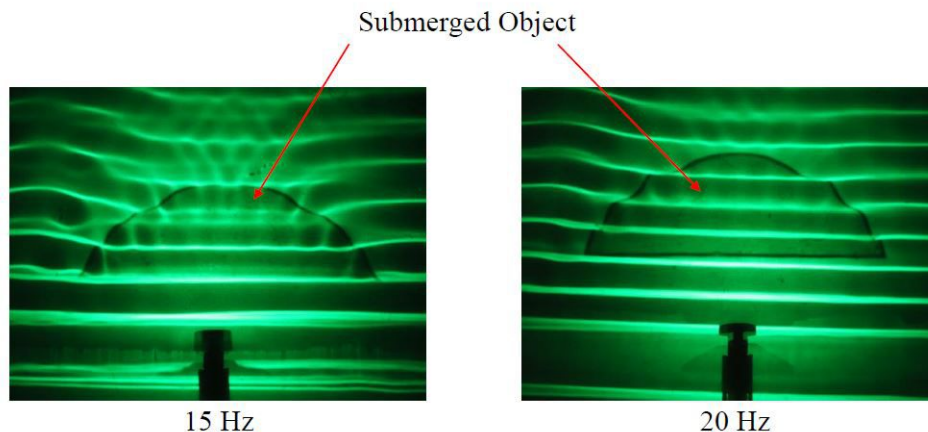

Figure 9: Two images showing the refraction of water waves at 15 Hz (left) and 20 Hz (right) as they pass over a submerged object.

Figure 10 is a selection of annotated images showing how the single-slit interference pattern of water waves varies with different gap widths.
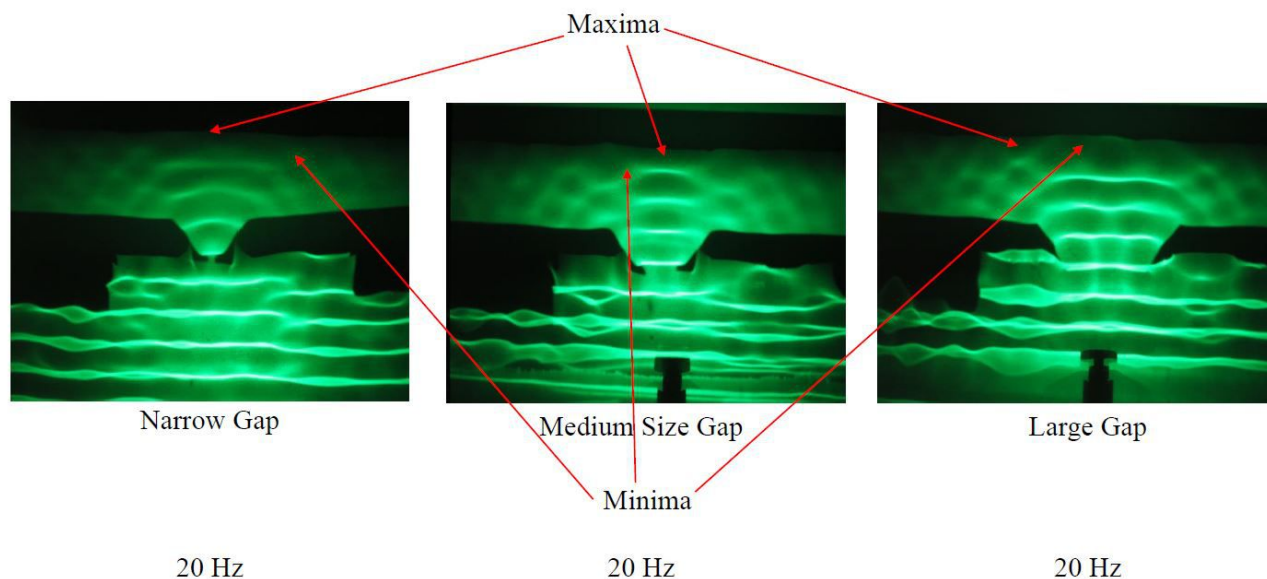

Figure 10: A selection of annotated images demonstrating how single-slit interference of water waves varies with gap width. Some maxima due to constructive interference and minima due to destructive interference are indicated.

Figure 11 shows two annotated images demonstrating how single-slit interference of water waves varies with different frequencies.
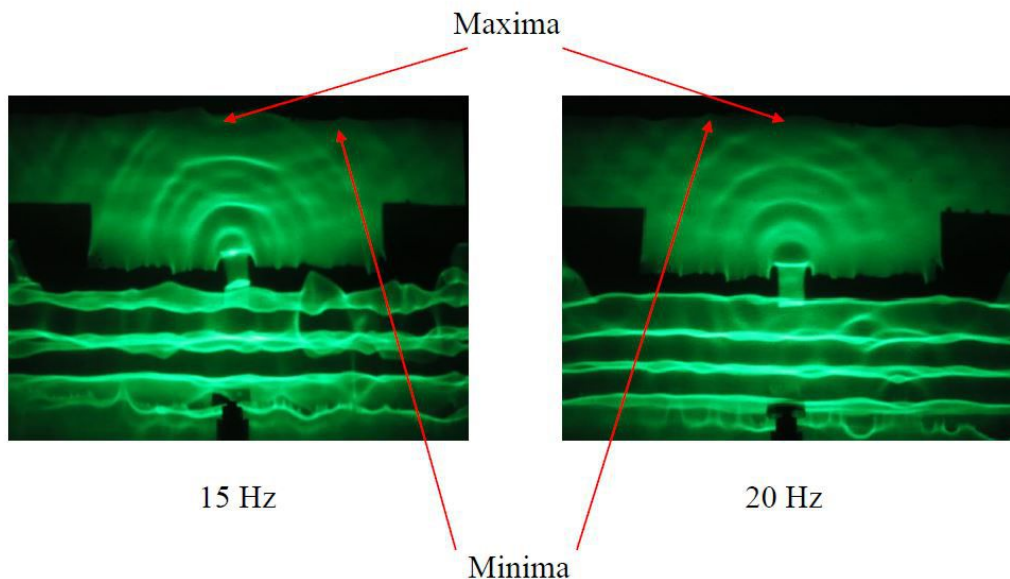
Figure 11: Single-slit interference of water waves at two different frequencies: 15 Hz shown left, and 20 Hz shown right. Some annotations have been included to indicate constructive interference (maxima) and destructive interference (minima).

Figure 12 demonstrates the Young's slits diffraction pattern generated from double-slit interference of water waves.
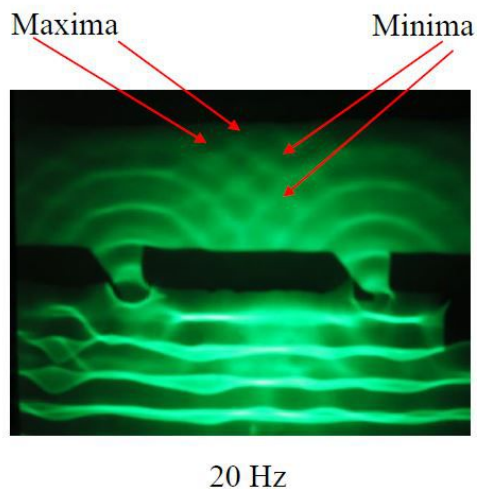

Figure 12: An annotated image demonstrating double-slit interference of water waves as they pass through two slits. The annotations highlight the maxima and minima formed due to the interference between the two wave fronts formed by the two slits.

Figure 13 shows how the wavelength of plane waves varies with depth due to the water tray positioned at a sloping gradient.

By using similar techniques to Figure 7 plane waves were analysed at various depths to produce Figure 14. This shows a plot of wave speed, v against the square-root of various depths, $\sqrt{h}$ of the water tray (not positioned at an angle) at a fixed frequency of 20 Hz.
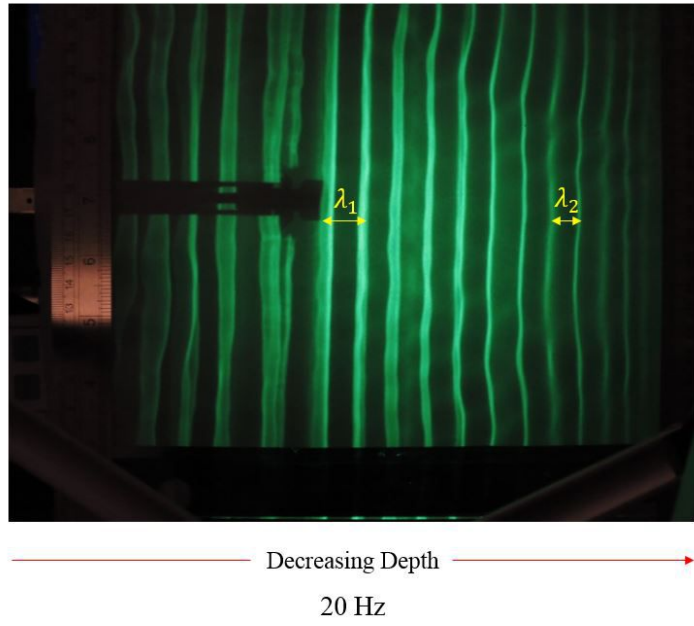
Figure 13: An image demonstrating qualitatively how the wavelength of plane waves varies with depth. The tray was angled such that the depth was decreasing in the direction of the propagating waves as indicated by the red arrow. Two wavelengths λ_1 and λ_2 are shown at deep and shallow points in the water tray respectively.
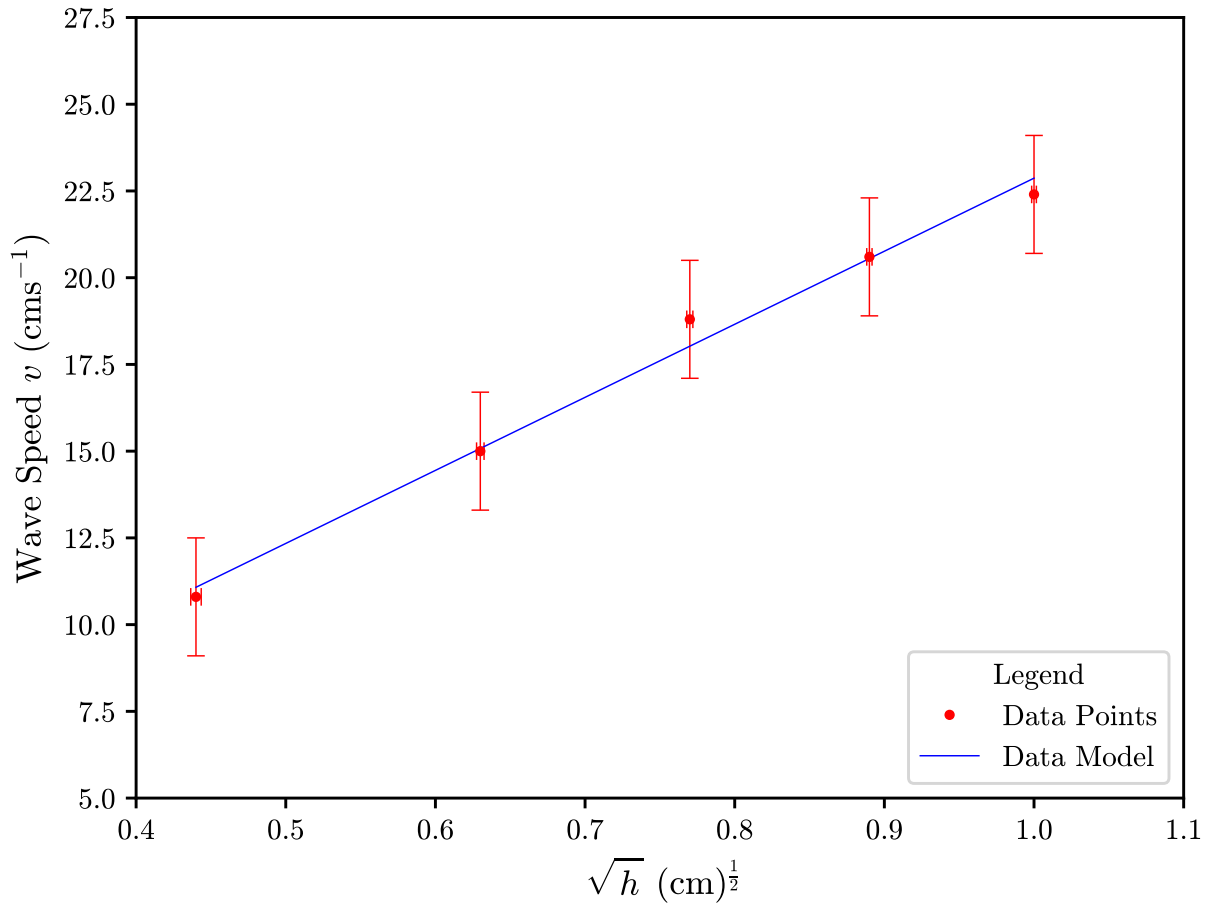

Figure 14: A plot of water wave speed, v against the square root of depth, $\sqrt{h}$ for a fixed frequency of 20 Hz.

From applying equation (4) an experimental value for the acceleration due to gravity, g could be determined from Figure 14 by obtaining the gradient and squaring it. The associated uncertainty was simply obtained by using the error in the gradient. Table 3 compares the experimental value of g obtained from Figure 14 to the accepted value.

Table 3: Table of values for the acceleration due to gravity, g.

Value	Acceleration Due to Gravity, $g(\mathrm{ms^{-2}})$
Experimental	4.4 ± 0.1
Accepted	9.8

4.2 Electromagnetic Waves

Figure 15 and Figure 16 show plots of intensity against screen position for the single slit configuration using a 0.3 mm aperture with slit widths of $a = 0.02$ mm and $a = 0.04$ mm respectively. Whereas, Figure 17 and Figure 18 show plots of intensity against screen position for the double slits configuration using a 0.3 mm aperture with a slit width of $a = 0.04$ mm and slit separations of $d = 0.25$ mm and $d = 0.5$ mm respectively.

Figure 19 and Figure 20 show plots of intensity against screen position for the single slit configuration using a different aperture of 1.0 mm with slit widths of $a = 0.02$ mm and $a = 0.04$ mm respectively. Figure 21 and Figure 22 show plots of intensity against screen position for the double slits configuration using a 1.0 mm aperture with a slit width of $a = 0.04$ mm and slit separations of $d = 0.25$ mm and $d = 0.5$ mm respectively.
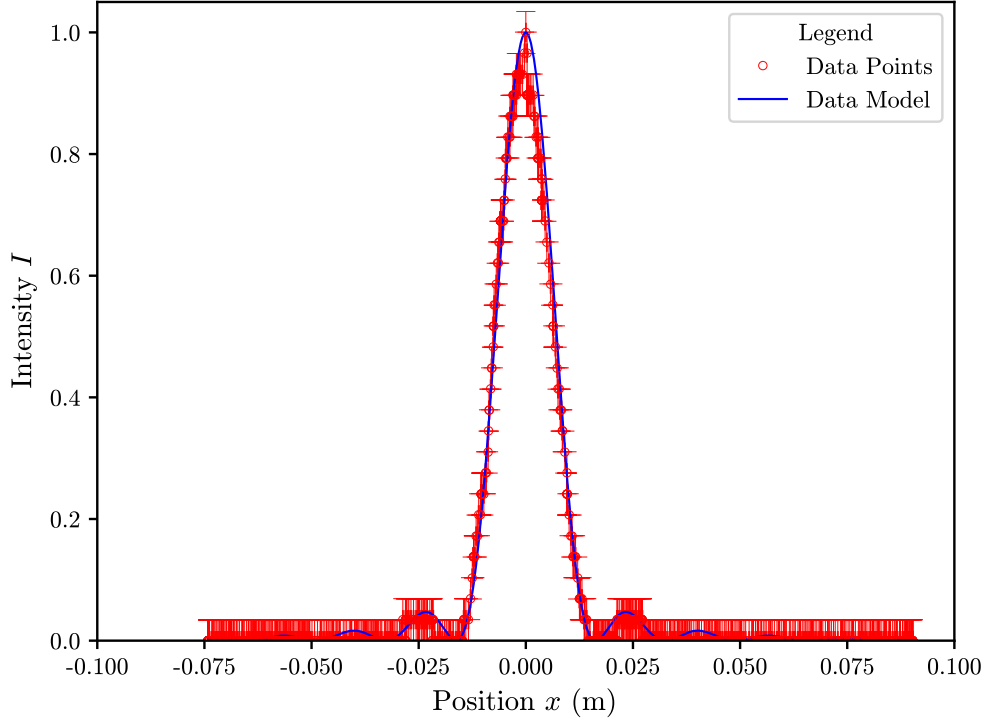
Figure 15: A plot of intensity, I against screen position, x for the single slit configuration with an aperture of 0.3 mm and slit width of $a = 0.04$ mm. An intensity function given by equation (8) is fitted to the data, as shown by the blue line.

Figure 16: A plot of intensity, I against screen position, x for the single slit configuration with an aperture of 0.3 mm and slit width of $a = 0.04$ mm. An intensity function given by equation (8) is fitted to the data, as shown by the blue line.
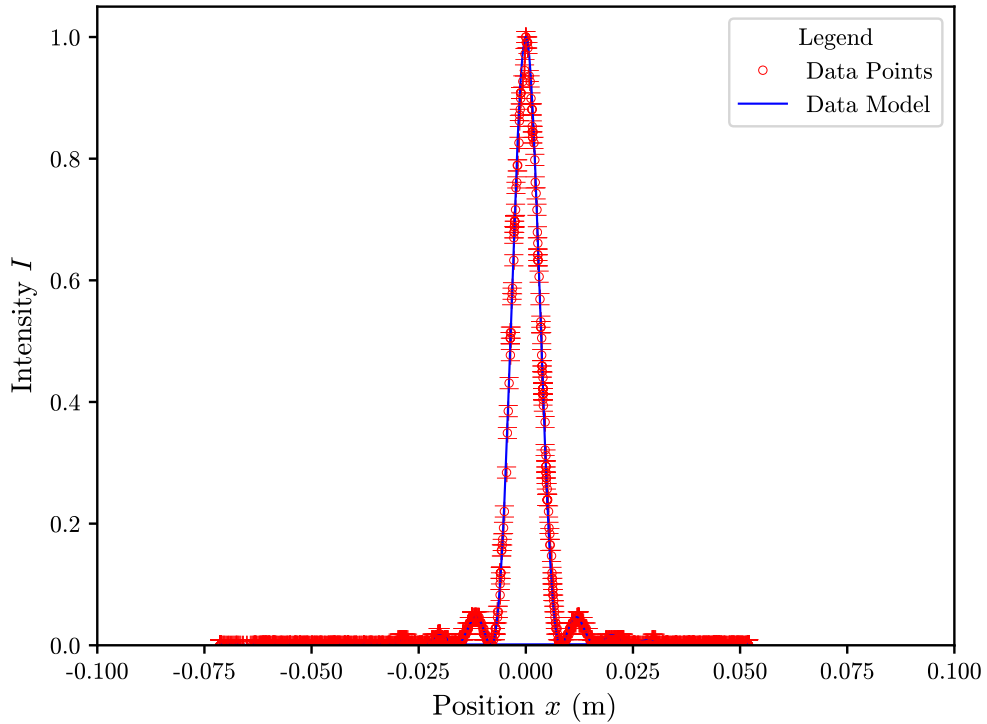
Figure 17: A plot of intensity, I against screen position, x for the double slits configuration with an aperture of 0.3 mm, slit width of $a = 0.04$ mm and slit separation of $d = 0.25$ mm. An intensity function given by equation (9) is fitted to the data, as shown by the blue line, and a single slit envelope using (8) is also plotted, shown by the dashed black line.

Figure 18: A plot of intensity, I against screen position, x for the double slits configuration with an aperture of 0.3 mm, slit width of $a = 0.04$ mm and slit separation of $d = 0.5$ mm. An intensity function given by equation (9) is fitted to the data, as shown by the blue line, and a single slit envelope using (8) is also plotted, shown by the dashed black line.

Figure 19: A plot of intensity, I against screen position, x for the single slit configuration with an aperture of 1.0 mm and slit width of $a = 0.04$ mm.. An intensity function given by equation (8) is fitted to the data, as shown by the blue line.
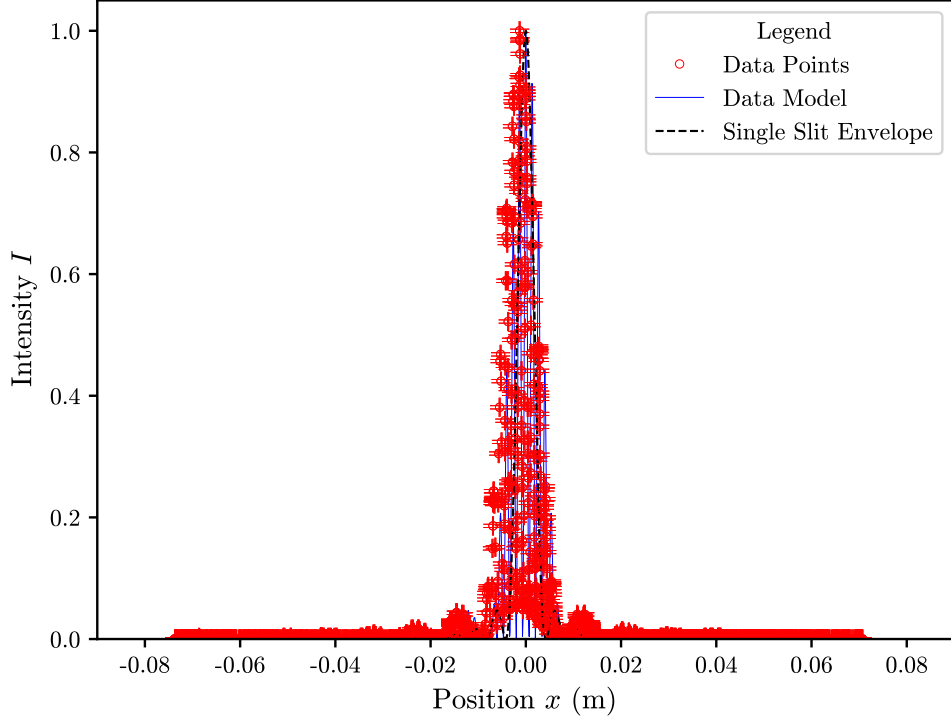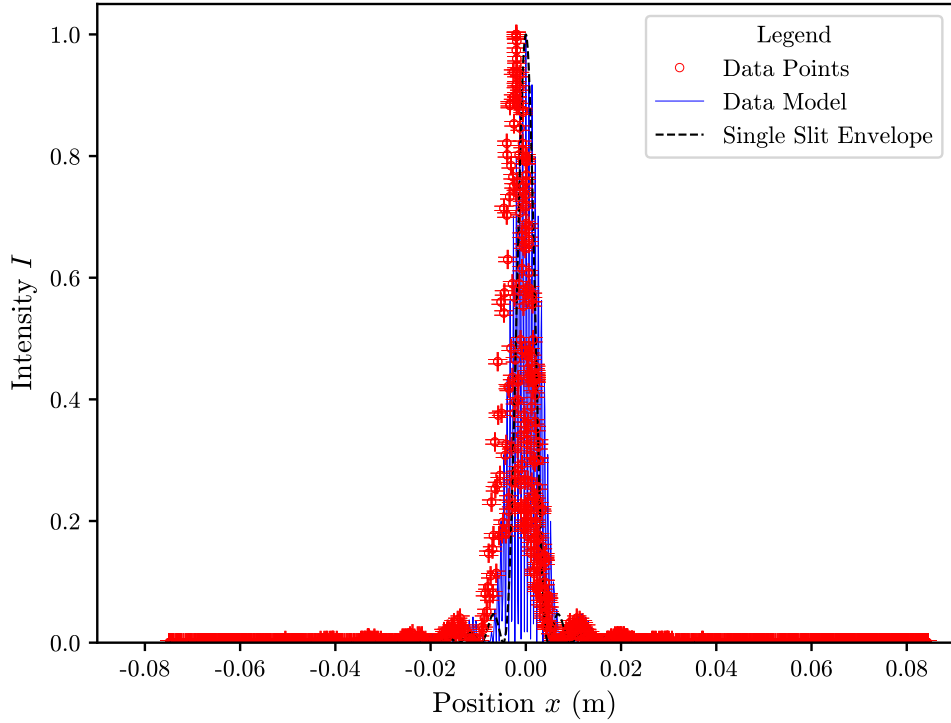

Figure 20: A plot of intensity, I against screen position, x for the single slit configuration with an aperture of 1.0 mm and slit width of $a = 0.04$ mm. An intensity function given by equation (8) is fitted to the data, as shown by the blue line.

Figure 21: A plot of intensity, I against screen position, x for the double slits configuration with an aperture of 1.0 mm, slit width of $a = 0.04$ mm and slit separation of $d = 0.25$ mm. An intensity function given by equation (9) is fitted to the data, as shown by the blue line, and a single slit envelope using (8) is also plotted, shown by the dashed black line.
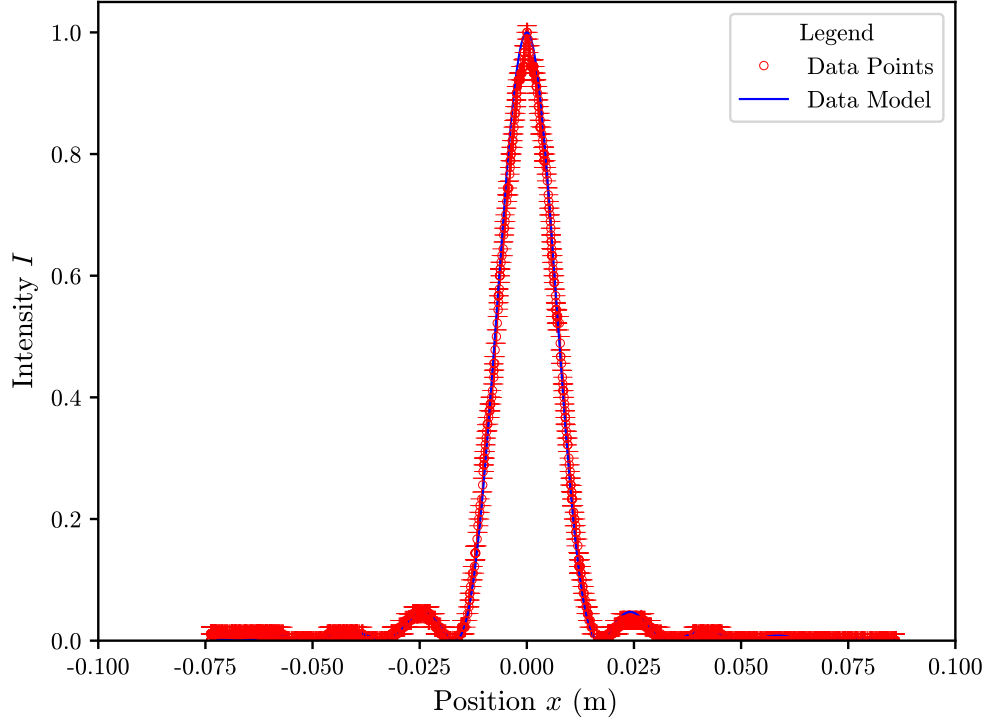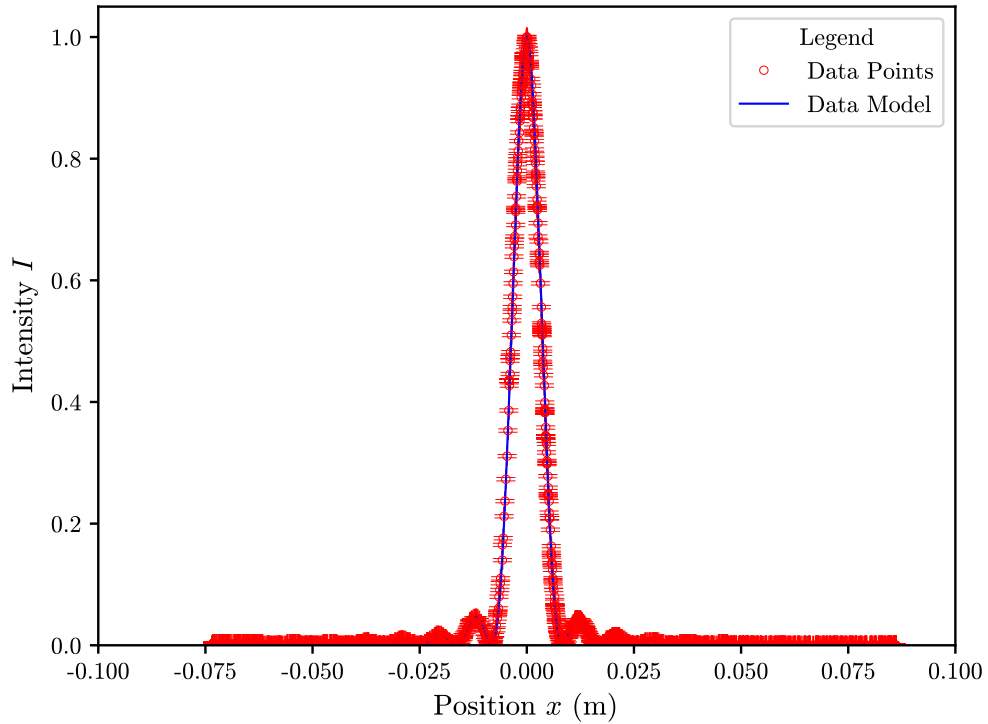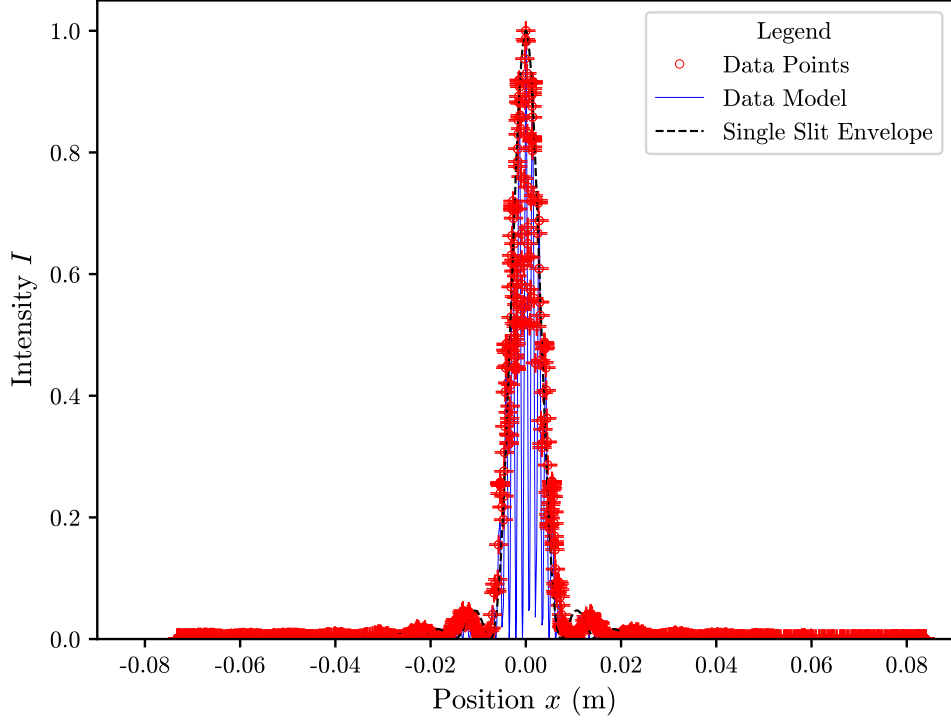

Figure 22: A plot of intensity, I against screen position, x for the double slits configuration with an aperture of 1.0 mm, slit width of $a = 0.04$ mm and slit separation of $d = 0.5$ mm. An intensity function given by equation (9) is fitted to the data, as shown by the blue line, and a single slit envelope using (8) is also plotted, shown by the dashed black line.
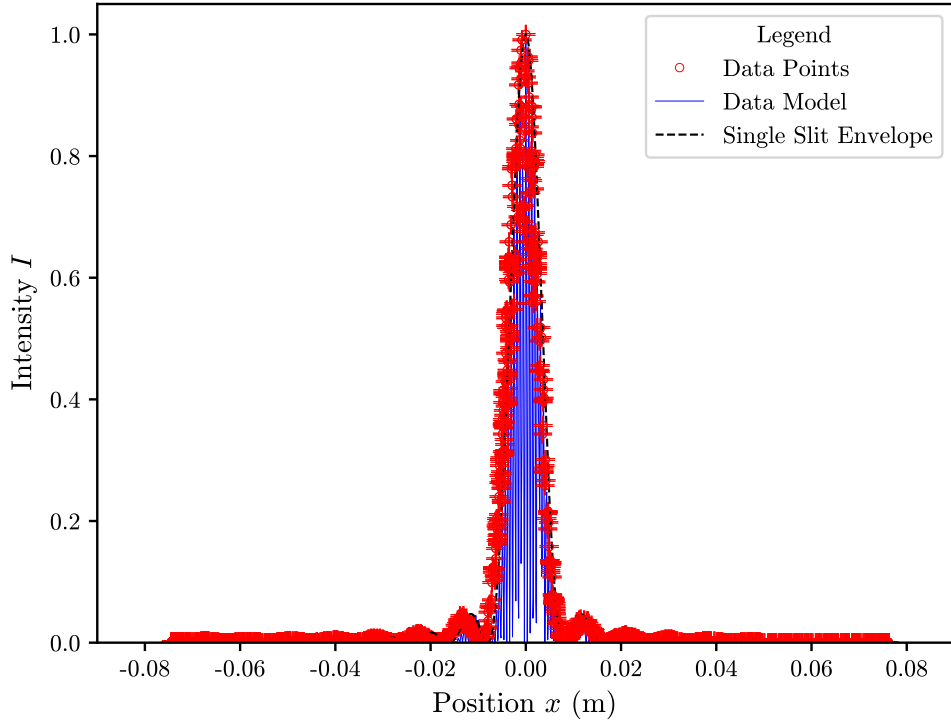
Table 4 shows the obtained values for the wavelength from the intensity function fitted to the diffraction patterns with the wavelength, λ as the only free parameter in equation (8) for the single slit intensity patterns.

Table 4: Table of experimental values for the wavelength, λ of the laser light source by using a non-linear least squares fit to the data with equation (8) for the single slit intensity patterns.

Aperture Size (mm)	Slit Width a(mm)	λ(nm) using (8)
0.3	0.02	652.1 ± 2.9
0.3	0.04	652.1 ± 0.7
1.0	0.02	674.0 ± 0.7
1.0	0.04	661.6 ± 0.2

Table 5 shows the obtained values for the wavelength from the intensity function fitted to the diffraction patterns with the wavelength, λ as the only free parameter in equation (9) for the double slit intensity patterns. In addition a single slit 'envelope' was also fitted to the double slit data by using equation (8) to obtain another experimental value for the wavelength of the laser light source.

Table 5: Table of experimental values for the wavelength, λ of the laser light source by using a non-linear least squares fitting routine to the data with equation (9) and using equation (8) to fit a single slit 'envelope' to the data for the double slit intensity patterns.

Aperture Size (mm)	Slit Width a(mm)	Slit Separation d(mm)	λ(nm) using (9)	'Envelope' λ_{env}(nm) using (8)
0.3	0.04	0.25	672.47 ± 0.04	338.5 ± 0.1
0.3	0.04	0.5	655.71 ± 0.03	378.0 ± 0.2
1.0	0.04	0.25	697.62 ± 0.03	599.3 ± 0.1
1.0	0.04	0.5	616.90 ± 0.01	645.4 ± 0.1

The errors in Table 4 and Table 5 were acquired using the error returned by the fitting function when the wavelength, λ was used as the only free parameter in equation (8) (single slit and 'envelope') and equation (9) (double slits).

Figure 23 is a selection of images comparing the single and double slit interference patterns for the mechanical and EM wave experiments.
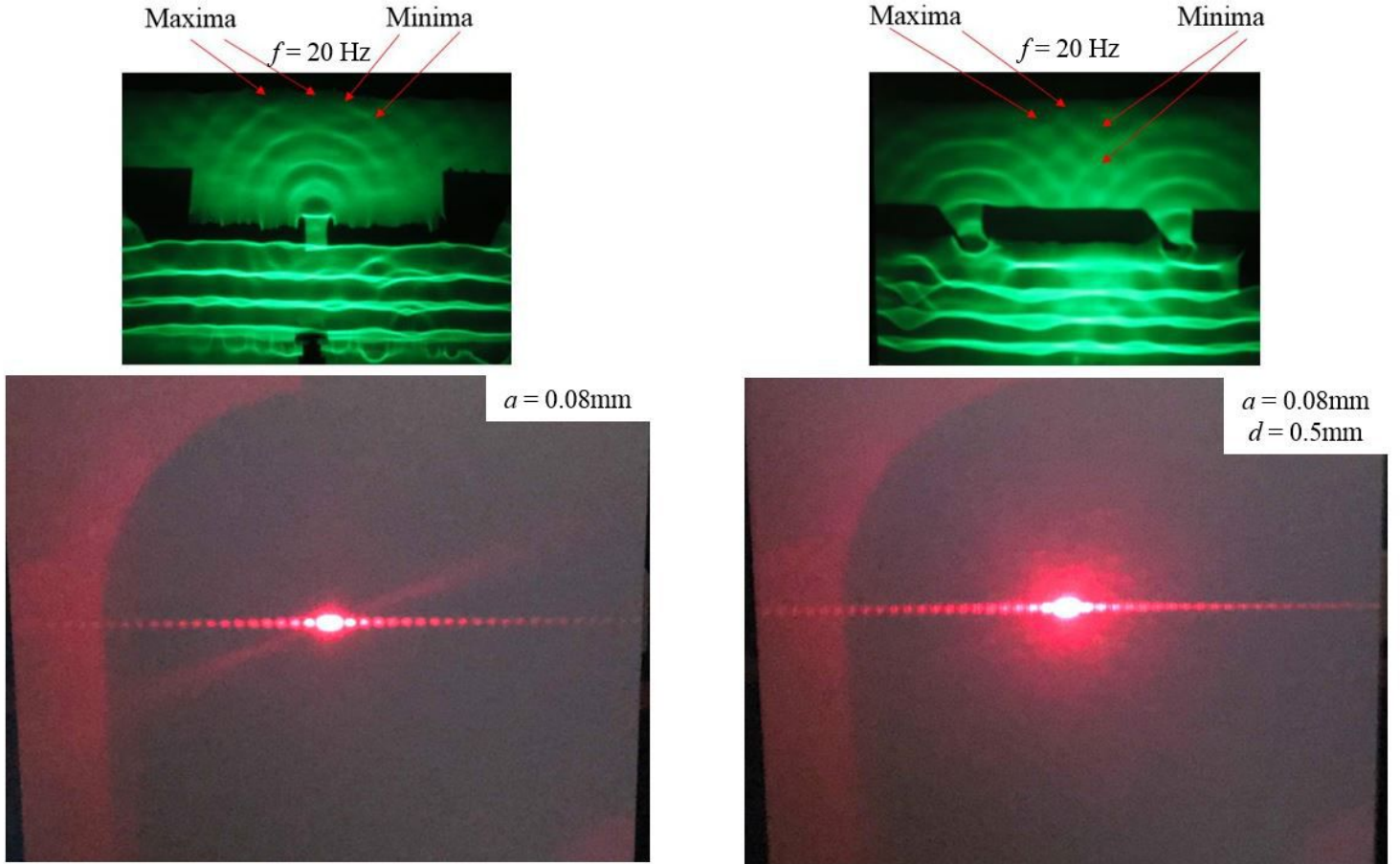

Figure 23: Images comparing the single (left) and double slit (right) interference patterns. The mechanical (water) waves interference patterns are shown by the top two images and the EM waves interference patterns are shown by the bottom two images.

5 Discussion

By analysing the images in Figure 6 at the frequencies of 15 Hz and 20 Hz it is clear to see that the wavelength of plane waves decreases with frequency as given by equation (3). Figure 7 also shows this trend of how wavelength increases with decreasing frequency with a fixed depth of $h = 1 \pm 0.3$ cm.

Comparing the results obtained from Figure 7 in Table 1 to the theoretical value, obtained by using equation (4) with a depth of $h = 1 \pm 0.3$ cm, there are some differences between the two values and the uncertainty ranges do not overlap with each other. The theoretical value in Table 1 has a large uncertainty associated with it. This was due to the difficulty in measuring the depth of the water with a ruler. It was hard to measure this accurately due to parallax and the difficulty in discerning the water level. Therefore, the value for the depth could not be accurately determined and the uncertainty associated with it was large. So, this impacted on the final theoretical result and associated error for the speed due to this large source of uncertainty in the propagation of equation (4). However, this was rectified for later experiments when measuring water waves speed as a function of depth where the depth was then measured using a vernier calliper mounted to a clamp stand to obtain more reliable values. Due to this inaccuracy of the obtained depth, the theoretical value in can therefore only be used as a rough comparison value for the value obtained from the gradient in Figure 7. The experimental value in Table 1 was hard to obtain due to the difficulty in measuring the wavelengths of the plane was at frequencies different from 20 Hz [1]. As shown in Figure 6 the image quality for the 15 Hz plane waves compared to the 20 Hz image is lower. This could be due to the intrinsic properties of the water waves and at frequencies different from 20 Hz they could start to interfere with the bottom of the water tank in unknown ways causing poor images to be obtained. Furthermore, the uncertainty in Table 1 for the experimental value for the wave speed was small due to underestimating the errors obtained in the wavelength when using the image processing programme. In reality, these distances were hard to obtain, due to the lack of clarity between pixel and 'real' distance. So, more consideration should have been taken when estimating these uncertainties in the image

wavelengths. Therefore, the uncertainty given for the experimental value of the wave speed in Table 1 is small due to the underestimated values in the image distances.

Figure 8 demonstrates nicely the wave properties of reflection due to a barrier placed at an angle. Some of the waves shown in Figure 8 have discrepancies in the quality of the image so the direction of the incoming and outgoing waves was slightly difficult to determine. Also the normal to the wave barrier was hard to construct due to the difficulty in observing the interface between the barriers and the wave fronts. However, this image and the results given in Table 2 show a good estimate to the angles of incidence, θ_i and reflection, θ_r. Furthermore, the results in Table 2 verify relation (5).

The refraction of water waves was hard to demonstrate and difficult to determine. Figure 9 shows that there is more refraction at lower frequencies than higher frequencies. This does not correspond with theory. It is generally known that waves travelling at a higher frequency (and hence a higher speed) refract more than those at lower frequencies. One of the reasons that may have caused this anomaly could be due to the properties of water waves. As mentioned previously, there may have been interactions between the water waves and the external environment, such as interference with the bottom of the water tank, that could have caused these unexpected effects with refraction at frequencies different to 20 Hz. In addition, only relatively small depths of water could be used due to a shallow tray. Therefore, because the speed of water waves depends on depth, the change in speed of the water waves as they pass over the submerged object would not have been big enough to ensure that noticeable refraction could occur and thicker objects could not be used to test this further due to these shallow depths.

Figure 10 nicely demonstrates how the single slit diffraction of water waves varies with gap width. The maxima and minima are clearly visible. As expected, at narrow gaps the water waves diffract more than those at larger gaps. In addition, Figure 11 shows that the diffraction of waters waves with a fixed gap width at two different frequencies evolve as one would expect. The 15 Hz image shows that the wavelength of the diffracted is bigger than those at 20 Hz. Figure 11 also shows that the diffraction patterns of the minima and maxima are more spread out at lower frequencies due to the larger wavelengths.

Furthermore, Figure 12 demonstrates qualitatively Young's slits diffraction pattern due to water waves passing through two gaps. The constructive and destructive interference regions are indicated. Also, the effects created by the interference due to the two wave fronts is nicely shown.

Water wave speed as a function of depth is shown in Figure 13; where the water tray was placed at an angle to vary the tray depth as indicated. This qualitatively demonstrates relation (4). Wave length is related to wave speed given by equation (3). Therefore, decreasing depths would also decrease the wavelength as expected by equations (3) and (4).

Quantitative analysis for the water waves as a function of depth was difficult to achieve. Table 3 shows that the experimental value for the acceleration due to gravity, g, is vastly different to the accepted value. The water depths were difficult to determine due to parallax errors and the capillary action acting between the water and the metal surface of the vernier calliper. So, the horizontal error bars given in Figure 14 are not accurately portrayed and should have been adjusted to account for these difficulties. In addition, the coefficient of friction was not taken into account between the bottom of the water waves and the surface of the tray. These frictional forces causes the water waves to move along their direction of travel. Equation (4) does not take this coefficient of friction into account. Therefore, all of this impacted on the final value obtained for g and this potentially led to the differences between the experimental and accepted values displayed in Table 3.

The single slit intensity equation (8) shows a strong corrlation to the data in Figure 15, Figure 16, Figure 19 and Figure 20. These single slit diffraction patterns closely correspond to those given in theory [5]. Furthermore, by comparing the diffraction patterns at different slit widths, a, for example the patterns using a 1 mm aperture - Figure 19 ($a = 0.02$ mm) and Figure 20 ($a = 0.04$ mm) - the pattern 'narrows' in as predicted by equation (8) for increasing slit widths. However, only narrow apertures (0.3 mm and 1.0 mm) could be used to investigate these diffraction patterns. This was due to limitations in the equipment with saturation in received intensity occurring at slit apertures bigger than 1.0 mm or for larger slit widths, a. Due to this limitation, further investigations could not be undertaken with bigger apertures and slit widths so more data could not be obtained to add more reliability to these diffraction patterns.

The experimental values obtained for the wavelength of the laser light source due to the single slit diffraction patterns shown in Table 4 compare well to the wavelength of the laser source of $\lambda = 650 \pm 10$ nm [8]. However, the uncertainties in Table 4 associated with these wavelength values are very small. This could be due to the fact that the width of the light sensor panel detecting the diffraction intensities was not taken into account. This detector could not determine accurately where the diffracted incident light interacts with the surface as it only measures the total amount of current produced by the panel as a result of the incident light. Therefore, the positions of the measured intensities would have a higher uncertainty associated with them due to this limitation in the experimental equipment. So, the horizontal error bars given in Figure 15, Figure 16, Figure 19 and Figure 20 would need to be increased to account for this. Furthermore, the width of the light sensor may have impacted on the received intensities at these positions. Hence, the uncertainties in the intensity (vertical error bars) would have needed to be increased to accommodate for this discrepancy. All of this would have led to a bigger uncertainty in the experimental values of the wavelength given in Table 4 obtained from the function (8) fit to the single slit data.

By observing Figure 17, Figure 18, Figure 21 and Figure 22 these double slit diffraction patterns correspond well to equation (9). These patterns show strong similarities to those given by theory theory [6]. Again the pattern narrows in but, this time

for increasing slit separation, d as predicted by equation (9). However, although the fitted function (9) fits reasonably well to the double slit diffraction patterns there are some discrepancies. This fitted function does not quite reach zero intensity in many regions within the first central maximum. This could be due to the resolution of the sensor not being taken into account for these measurement. So, the positions of the minimum could not be accurately determined due to this limitation. Also, similar to the single slit experiments, problems occurred with saturation of the intensities at slit apertures greater than 1.0 mm or at large slit widths, a for the double slit configuration. Therefore, more data could not be obtained to verify these evolution of these patterns for different experimental configurations.

Furthermore, by comparing the values obtained for the wavelength in Table 5 to the value of the laser device of $\lambda = 650 \pm 10$ nm they compare fairly well. Again, there are small uncertainties associated to these wavelengths. As mentioned previously, this could be due to the fact that the resolution of the detector was not taken into account during the experiment. In addition, the values of the wavelength obtained from the single slit envelope for the 0.3 mm aperture are almost half that of the laser device value. By inspecting Figure 17 and Figure 18 this is due to the single slit function (8) not fitting well to the data. These two figures clearly show that the single slit envelope is slightly 'skewed' from the data points and this has therefore impacted on the values obtained for the wavelength, λ_{env}, given in Table 5.

Figure 23 shows a nice comparison between the interference patterns of mechanical and electromagnetic waves. The single slit diffraction patterns for the water waves clearly indicate constructive (maxima) and destructive (minima) interference. The single slit diffraction pattern for the EM waves indicates clear resemblance to the water wave interference pattern with bright regions indicating constructive interference and dark regions indicating destructive interference. Furthermore, Figure 23 shows strong parallels between mechanical and EM wave double slit interference patterns. Regions of constructive and destructive interference are clearly shown by the water waves due to the slits. Although difficult to see due to the resolution and quality of the image there are regions of destructive interference between the constructive regions shown as 'splittings' in the diffraction pattern for the EM waves image. This shows strong similarities to Figure 17, Figure 18, Figure 21 and Figure 22 where the destructive regions are shown as low intensity readings in between the high intensity measurements indicated by the blue data model (using equation (9)) plotted in these figures.

6   Conclusion

Overall the images in Section 4.1 show that water waves nicely demonstrate various properties of (mechanical) waves. Although it was hard to demonstrate the refraction of water waves in Figure 9 due to the difficulty in viewing a significant change in the wave speed, other wave properties such as how wave speed varied with frequency, reflection, single and double-slit interference were successfully observed. In addition, it has qualitatively been shown that the water wave speed does increase with depth given by Figure 13 and this feature has also been illustrated quantitatively with a plot of wave speed, v against the square-root of depth, $\sqrt{h}$ in Figure 14. Furthermore, the diffraction graphs for the single and double-slit interference patterns of EM waves shown in Section 4.2 nicely show how the diffraction patterns evolve with changing slit width a and slit separation d. Even though there were discrepancies in estimating the uncertainties for the experimental values of the wave length for the laser light source the values given in Section 4.2 Table 4 and Table 5 give good results that correspond fairly well with the one given for the device of $\lambda = 650 \pm 10$ nm [8]. By studying the interference patterns the wavelengths of unknown light sources maybe able to be determined. Therefore, this technique could be used as a 'finger printing' processes that uses wavelengths to identify specific chemical elements, for example chemical spectra analysis of astronomical objects. Lastly, Figure 23 shows that the mechanical and EM waves interference patterns behave similarly for the single and double-slit configurations. This further indicates that the physics of waves is the same regardless whether water waves, sound waves, EM waves, etc are considered. Therefore, by investigating the properties of EM waves these could be transferred to water waves to enhance them for new applications such as devising more efficient methods of generating hydroelectric power.

References

[1] College of Engineering Mathematics and Physical Sciences, University of Exeter, PHY2026, *Waves in a Ripple Tank Worksheet* (Accessed 8th February 2019).

[2] College of Engineering, Mathematics and Physical Sciences, University of Exeter, PHY2026, *Diffraction and Interference Worksheet* (Accessed 8th February 2019).

[3] Young, Hugh D and Freedman, Roger A, *University Physics*, 13th Edition, 2014, Chapter 36, pages 1312 - 1322.

[4] Barber N.F, *Water Waves*, 1st Edition, 1969, Chapter 3, pages 36 - 55.

[5] Pedrotti F.L, Pedrotti S.J, *Introduction to Optics*, (Pearson International Edition) 3rd Edition, 2006, Chapter 11-1: *Diffraction from a Single Slit*, pages 268 - 273.

[6] Pedrotti F.L, Pedrotti S.J, *Introduction to Optics*, (Pears onInternational Edition) 3rd Edition, 2006, Chapter 11-5: *Double-Slit Diffraction*, pages 281 - 284.

[7] *Fraunhofer Diffraction*, `http://people.ucalgary.ca/~lvov/471/labs/fraunhofer.pdf` (Accessed 9th February 2019.)

[8] *Red Diode Laser - Basic Optics - OS-8525A*, `https://www.pasco.com/prodCatalog/OS/OS-8525_red-diode-laser-basic-optics/index.cfm?fbclid=IwAR3gzuNSAoumEZpwYZQO6tX3j1nLhTtLYklX5U6V6HHw5xyHKdszO1ID00I` (Accessed 15th March 2019).